RSC Advances

PAPER

View Article Online
View Journal | View Issue

Cite this: *RSC Adv.*, 2025, **15**, 47826

Fe_3O_4/cellulose/Zn-MOF: introduction of a new catalyst for the synthesis of tetrazolo[1,5-*a*] pyrimidine-6-carbonitriles and diphenyl-1,3-thiazoles under solvent-free conditions

Maryam JahangirVazifeh,[a] Mohammad Hossein Abdollahi-Basir,[a] Bahman Sharifzadeh[b] and Farhad Shirini *[a]

Received 18th September 2025
Accepted 13th November 2025

DOI: 10.1039/d5ra07068f

rsc.li/rsc-advances

In this research, a novel, magnetically recoverable heterogeneous catalyst, Fe_3O_4/cellulose/Zn-MOF, was synthesized and thoroughly characterized using EDX, EDX mapping, FT-IR, SEM, TGA, XRD, and VSM to determine its physicochemical properties. Then, its catalytic activity was explored through one-pot, solvent-free, three-component reactions for the synthesis of diphenyl-1,3-thiazoles and tetrazolo[1,5-*a*] pyrimidine-6-carbonitriles. The system exhibited several outstanding properties, including excellent recyclability (over 5 successive rounds), low catalyst loading, remarkable product purity and yield, and a simplified work-up procedure, rendering it a promising candidate from a green chemistry perspective.

Introduction

Owing to the multi-functionality introduced by multiple coating layers, core–shell nanostructures that can tune structural properties have attracted considerable attention.[1–3] These coating layers enable the modification of chemical properties, augment aggregate stability, and amplify the inner core's catalytic activity. Moreover, increasing the number of shells extends their functional versatility, making them applicable in a wide range of fields, including medicine, therapy, and catalysis.[4–7]

Over the past few decades, a great deal of research has been conducted on the role of heterogeneous catalysts in diverse organic reactions, mainly due to their industrial relevance and eco-friendly attributes. One of their notable advantages lies in their recoverability and ease of separation from the product. However, as heterogeneous catalysts operate in a different phase than the reactants, as opposed to their homogeneous counterparts, their catalytic performance tends to diminish over time, resulting in a decline in total reaction efficiency.[8–13]

The fabrication of heterogeneous catalysts from organic–inorganic hybrid materials has gained attention due to their flexibility, structural diversity, and improved thermal and mechanical stability.[14–17] Nano-sizing these catalysts (1–100 nm) enhances their catalytic quality by increasing the active surface area, resulting in increased catalytic reactivity.[18–20] From a green chemistry standpoint, new catalyst recycling methods are needed to replace traditional filtration and centrifugation.[21–27] Magnetic nanocatalysts (NCs) have emerged as promising candidates, owing to their facile and rapid separation from liquid media under the effect of an external magnetic field. Among them, Fe_3O_4 NCs are especially advantageous due to their low toxicity, reusability, environmental friendliness, strong thermal and chemical [tension] stability, large surface area, high scalability, and cost-effectiveness. Their synthesis *via* co-precipitation positions them as ideal supports for catalysts.[28–30]

Despite their wealth of remarkable attributes for multiple applications,[31,32] magnetic nanoparticles (MNPs) pose significant challenges in removal from suspensions due to their propensity for aggregation and susceptibility to oxidation, which limits their usability. Consequently, researchers have explored diverse methods to mitigate these drawbacks, including polymeric templating during *in situ* synthesis of MNPs, their functionalization, and the engineering of polymer composites.[33] Among these, nanocellulose stands out as an exceptional candidate due to its notable features, particularly the hydroxyl groups that foster hydrogen-bonding networks, facilitating the condensation of MNPs within a nanofiber network. Magnetic nanocellulose composites (MNCs) comprising Fe_3O_4 NPs exhibit superparamagnetism and find extensive applications in biomedicine, ranging from MRI diagnostics, disease treatment, biosensing, and biolabeling to controlled drug release,[34–38] as well as environmental solutions, including water purification, filtration, adsorbents, photocatalysis, and fuel cells.[39,40]

Defined as hybrid organic–inorganic systems, metal–organic frameworks (MOFs) consist of metal ion/cluster centers

[a]*Department of Organic Chemistry, Faculty of Chemistry, University of Guilan, Rasht, 41335-19141, Iran. E-mail: shirini@guilan.ac.ir; fshirini@gmail.com; Fax: +98 131 3233262; Tel: +98 131 3233262*

[b]*Department of Inorganic Chemistry, Faculty of Chemistry, University of Guilan, Rasht, 41335-19141, Iran*

coordinated to organic ligands, assembling into crystalline and space-coherent porous lattices that exhibit diverse physical and chemical properties.[41] Their structural characteristics, *e.g.*, high surface area, thermal stability, large porosity, and pore/lattice functionality, have propelled MOFs into numerous biomedical and environmental applications, including catalysis, sensing, and adsorption of metal ions and toxic gases.[42] Among these, catalytic applications are especially vital, serving as foundational processes in manufacturing a wide range of products from basic chemicals to agrochemicals, cosmetics, foodstuffs, pharmaceuticals, petrochemicals, and polymers. The magnitude of research in this area is evidenced by nearly 8000 journal articles and over 100 patents concerning MOF-based catalysis reported in recent decades.[43] The inherent flexibility of MOF materials stemming from the wide selection of organic/inorganic components renders them particularly well-suited for applications in fine chemistry.[44,45] However, they are not commonly used in catalyzing organic coupling reactions.[46,47] A major focus within the field of catalysis lies in the formation of C-heteroatom and C–C bonds, given their pivotal role in constructing high-value products. The employment of MOFs as green catalysts has been shown to expedite organic reactions. As supported by prior authoritative articles, the metal ions in MOF structures function as Lewis acids, while the carboxylate anions serve as Lewis bases. In this dual capacity, Zn-MOFs have been deployed as bifunctional catalysts owing to the simultaneous presence of carboxylate anions and metal cation sites (Zn^{2+}).[48]

In response to escalating global environmental challenges and within the framework of green chemistry, it has become imperative to employ catalysts, eschew hazardous chemical solvents, and minimize the generation of chemical wastes in organic reactions. Among the strategies aligned with these objectives, multi-component reactions (MCRs) have emerged as particularly potent methodologies for synthesizing certain chemical compounds. This is because MCRs have taken more prominence over multi-step reactions, most importantly for being cost-effective, time-saving, low-energy-consuming, and synthetically convergent. In this line, solvent-free MCRs have garnered chemists' attention, particularly from a green chemistry perspective.[49,50] The merits of such an approach include diminished waste production, ease of operation, mild reaction conditions, enhanced selectivity, and superior overall efficiency.[51] A few notable reactions of this sort include the synthesis of diphenyl-1,3-thiazoles and tetrazolo[1,5-*a*]pyrimidine-6-carbonitriles.

The incorporation of fused polyheterocycles is widely regarded as central to the architecture of numerous natural products and pharmaceuticals. Their broad utility, particularly in the domain of drug discovery, has motivated chemists to extensively synthesize them. Pyrimidines and associated nitrogen-containing heterocyclic derivatives (*e.g.*, tetrazolopyrimidines) have garnered considerable scientific focus toward their biological applications. Many compounds featuring a tetrazole moiety have been characterized as potent xanthine oxidase inhibitors,[52] antitubercular agents,[53] antimicrobial agents,[54] and antinociceptive agents.[55] Among heterocycles, thiazole-based heterocycles—specifically 1,3-thiazoles, *i.e.*, five-membered heterocyclic aromatic rings containing sulfur and nitrogen heteroatoms—are characterized by their vast array of biological activities and are dominant heterocycles extensively used in drug design and synthetic chemistry. The remarkable pharmacological relevance of 1,3-thiazole-based compounds has driven a surge in the design and synthesis of 1,3-thiazole derivatives with promising activity profiles across therapeutic categories such as analgesic, anticancer, antibacterial, antidiabetic, anti-inflammatory, antifungal, antioxidant, antiviral, and antiprotozoal domains.[56]

Considering the environmental impact of chemical synthesis, this research presents a novel, environmentally friendly magnetic nanocomposite, containing imidazole, Fe_3O_4, cellulose, and Zn-MOF (Fe_3O_4/cellulose/Zn-MOF), as a heterogeneous and recyclable catalyst for the synthesis of two pharmaceutically significant heterocyclic compounds—diphenyl-1,3-thiazoles and tetrazolo[1,5-*a*]pyrimidine-6-carbonitriles—through a one-pot, three-component reaction conducted at 120 °C under solvent-free conditions. In this catalytic system, the reaction between barbituric acid or *N*,*N*′-dimethylbarbituric acid with aryl glyoxal and aryl thioamides efficiently produces diphenyl-1,3-thiazoles. Likewise, the condensation of aromatic aldehyde, 3-cyanoacetylindole, and 1*H*-tetrazole-5-amine affords tetrazolo[1,5-*a*]pyrimidine-6-carbonitriles. The process enables easy access to the target products in excellent yields with significantly short reaction times. The magnetic nature of this nanocomposite enables facile separation through an external magnet as well as efficient recovery, allowing it to be reused for up to five cycles with no loss of catalytic performance. This opens up the possibility of improving its sustainability profile, thus making it highly suitable for industrial applications.

Experimental

Material and instrumentation

All chemicals (reagents and solvents) were obtained from Sigma-Aldrich, Merck, and Fluka, and were used as received without any further purification. Product identities were confirmed by comparison of spectral data and melting points with those reported in the literature. Reported yields correspond to the isolated products. Reaction monitoring and assessment of substrate purity were performed *via* TLC using silica gel plates (POLYGRAM SILG/UV254). Melting points were determined using an IA9100 electrothermal digital melting point apparatus in capillary tubes. FT-IR spectra were recorded on a VERTEX 70 spectrometer (Bruker, Germany) by utilizing KBr pellets for the resulting solid samples. XRD analyses were carried out using an X'Pert Pro diffractometer (PANalytical, Netherlands). FESEM was performed on a Sigma VP instrument (TESCAN, ZEISS, Germany). TGA was conducted on a METTLER TGA/SDTA 851 thermal analyzer (Switzerland). EDS was carried out using a TESCAN MIRA III system (France).

Synthesis of Fe_3O_4

A previously reported procedure was adopted to prepare Fe_3O_4 magnetic nanoparticles (MNPs).[57] In addition,

superparamagnetic particles were synthesized through the co-precipitation of Fe^{2+} and Fe^{3+} ions in a 28 wt% NH_4OH solution, and then subjected to hydrothermal treatment. In brief, 5 g of $FeCl_3 \cdot 6H_2O_3$ and 2.6 g of $FeSO_4 \cdot 7H_2O$ were dissolved in distilled water (93 mL). Ammonia (69 mL) was added to this solution, leading to the immediate formation of a solid precipitate under vigorous stirring at 25 °C. The solution was then heated and maintained at 80 °C for 30 min. Afterward, the Fe_3O_4 nanoparticles were separated by applying an external magnet and repeatedly washed with deionized water. The resulting black Fe_3O_4 MNPs were vacuum-dried at 70 °C (98%).

Synthesis of Fe_3O_4/cellulose nanocomposite

In this study, the Fe_3O_4/cellulose nanocomposite was first fabricated according to a previously described procedure.[58] For this purpose, 0.15 g of Fe_3O_4 nanoparticles was dispersed in an aqueous solution (30 mL) containing 7 wt% NaOH and 12 wt% urea, then cooled to −12 °C for one hour. Then, 0.1 g of cellulose was added, and the mixture was stirred for 15 min. After an additional freezing for one hour, the cellulose fully dissolved. The addition of deionized water then induced the formation of the Fe_3O_4/cellulose nanocomposite. This product was magnetically collected (using an external magnet), washed with deionized water, and vacuum-dried at 70 °C (97%).

Synthesis of Fe_3O_4/cellulose/Zn-MOF

First, 0.2 g of Fe_3O_4/cellulose was dispersed in 60 mL of DMF and sonicated for 20 min to achieve complete dissolution. Then, for the reagents to dissolve, 1,4-benzenedicarboxylic acid (0.033 g, 0.20 mmol), imidazole (IM) (0.136 g, 2 mmol), and $Zn(NO_3)_3 \cdot 6H_2O$ (0.079 g, 0.26 mmol) were introduced into the mixture and sonicated for an additional 15 min. The sealed reaction vessel was stirred at 120 °C for 48 h. Upon cooling to ambient temperature, the resulting dark brown precipitate was separated with an external magnet, washed with ethanol, and vacuum-dried at 70 °C (0.426 g, 95%, Scheme 1).

General procedure for the synthesis of tetrazolo[1,5-*a*] pyrimidine-6-carbonitrile (4a–4m)

An equimolar three-component reaction involving aromatic aldehyde, 3-cyanoacetyl indole, and 1*H*-tetrazole-5-amine was carried out under solvent-free conditions at 120 °C in the presence of Fe_3O_4/cellulose/Zn-MOF (0.02 g) for an appropriate duration. The reaction was monitored by TLC (*n*-hexane : ethyl acetate = 3 : 1). Upon completion, the mixture was cooled down to room temperature and diluted with 15 mL of dichloromethane, followed by stirring for an additional 10 min to ensure complete dissolution of the product. The catalyst was then separated with an external magnet. Upon solvent evaporation, the crude product was recrystallized from ethanol to furnish pure tetrazolo[1,5-*a*]pyrimidine-6-carbonitriles, which were characterized by comparing their melting points and ^{13}C-NMR and ^{1}H-NMR spectral analyses.

The spectral data of the new product are as follow: 5-(1*H*-indol-3-yl)-7-(3-nitrophenyl)tetrazolo[1,5-*a*]pyrimidine-6-carbonitrile (**4m**): yellow solid; Mp: 283–285 °C; ^{1}H NMR (250 MHz, DMSO-d_6): δ: 7.26 (s, 2H, Ar–H), 7.53 (s, 1H, Ar–H), 7.79 (m, 2H, Ar–H), 8.27 (s, 1H, Ar–H), 8.34 (m, 1H, Ar–H), 8.40 (m, 1H, Ar–H), 8.55 (s, 1H, Ar–H), 11.11 (s, 1H, NH) ppm; ^{13}C NMR (62.9 MHz, DMSO-d_6): δ: 103.7, 112.7, 112.8, 113.2, 114.3, 118.3, 121.9, 123.2, 124.3, 126.6, 131.2, 133.4, 137.4, 138.1, 139.2, 150.4, 151.3, 157.9, 159.2, 159.4 ppm.

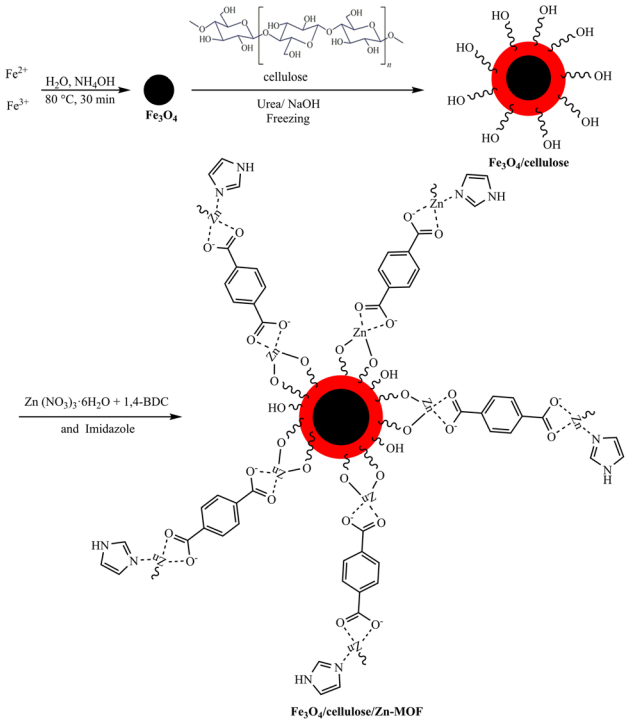

Scheme 1 Preparation of the Fe_3O_4/cellulose/Zn-MOF.

General procedure for the synthesis of diphenyl-1,3-thiazoles (4a–4l)

Under solvent-free conditions, 1 mmol each of barbituric acid and/or *N*,*N*′-dimethylbarbituric acid, aryl glyoxal, and aryl thioamides were mixed with 0.05 g of Fe_3O_4/cellulose/Zn-MOF and heated for an appropriate duration in an oil bath at 120 °C. The reaction was tracked using TLC (*n*-hexane : ethyl acetate (6 : 2)). After the starting materials had entirely disappeared, the mixture was cooled, to which 10 mL of hot dichloromethane was added. Due to the catalyst's insolubility in dichloromethane, the catalyst was separated using an external magnet. Finally, following solvent evaporation, the resulting solid was filtered, cooled down, and washed with cold diethyl ether and water. After drying, the product was recrystallized from absolute ethanol and identified by comparing its melting point and ^{13}C-NMR and ^{1}H-NMR spectral analyses.

The spectral data of the new product are as follow: 5-(2-(4-bromophenyl)-4-phenylthiazol-5-yl)-6-hydroxypyrimidine-2,4(1*H*,3*H*)-dione (**4h**): pale yellow solid; Mp: 311–313 °C; ^{1}H NMR (250 MHz, DMSO-d_6): δ: 4.28 (s, 1H, OH), 7.26 (s, 1H, Ar–H), 7.46–7.47 (m, 3H, Ar–H), 7.59–7.71 (m, 4H, Ar–H), 8.10 (d, 2H, Ar–H), 11.46 (s, 2H, NH) ppm; ^{13}C NMR (62.9 MHz, DMSO-d_6): δ: 81.95, 114,28, 118.38, 122.86, 123.75, 124.59, 125.57, 131.00,

133.68, 136.09, 144.04, 148.97, 149.17, 151.82, 153.61, 161.67 ppm.

Results and discussion

Catalyst characterization

Fig. 1 illustrates the SEM images of Fe_3O_4, Fe_3O_4/cellulose, and Fe_3O_4/cellulose/Zn-MOF. Fig. 1a shows that Fe_3O_4 nanoparticles are spherical with an average size of 20 nm. The Fe_3O_4/cellulose particles maintain the fundamental morphological characteristics of Fe_3O_4 but have increased particle size (about 25–30 nm), greater agglomeration, and a smoother surface (Fig. 1b). The Fe_3O_4/cellulose/Zn-MOF nanocomposite shows mean particle sizes in the range of 35–45 nm (Fig. 1c). These observations confirm the successful synthesis of the nanocatalyst, as evidenced by the changes in particle size and agglomeration.

The XRD technique provides valuable information, including crystalline structure, product purity, and phase identification. The XRD patterns of Fe_3O_4, cellulose, Fe_3O_4/cellulose, and Fe_3O_4/cellulose/Zn-MOF are displayed in Fig. 2. The analysis of the Fe_3O_4/cellulose nanocomposite's XRD pattern reveals that Fe_3O_4 NPs' crystalline structure is essentially maintained upon their congregation onto the surface of cellulose. The XRD pattern of Fe_3O_4/cellulose exhibits seven diffraction peaks at $2\theta = 22.70$, 30.5, 35.24, 43.20, 53.59, 57.13, and 62.76°, ascribing to the crystal plane diffraction peaks of the (113), (220), (311), (400), (422), (511), and (440) of Fe_3O_4 nanoparticles. The XRD pattern of Fe_3O_4/cellulose/Zn-MOF displays that visible diffraction peaks at about $2\theta = 6.88$, 10.58, and 14.98° are assigned to the characteristic diffraction peaks of Zn-MOF. The visibility of sharp peaks in the XRD patterns of the samples corroborates that the synthesized Fe_3O_4/cellulose/Zn-MOF is of high crystallinity. These results verify the catalyst's phase purity, as no impurity-related characteristic peaks are visible in the obtained patterns.

Energy-dispersive X-ray spectroscopy (EDX) was employed to characterize Fe_3O_4/cellulose/Zn-MOF, thereby confirming its composition. Fig. 3 illustrates that the synthesized nanocomposite is composed exclusively of carbon (C), nitrogen (N), oxygen (O), zinc (Zn), and iron (Fe) elements. Moreover, EDX elemental mapping was conducted on Fe_3O_4/cellulose/Zn-MOF (Fig. 4). The uniform distribution of elements confirmed the absence of impurities within the structure of the synthesized nanocomposite. As shown in Fig. 4a–e, the catalyst exhibited remarkable purity and a homogeneous elemental distribution of C, Fe, N, O, and Zn within its framework (Fig. 4f).

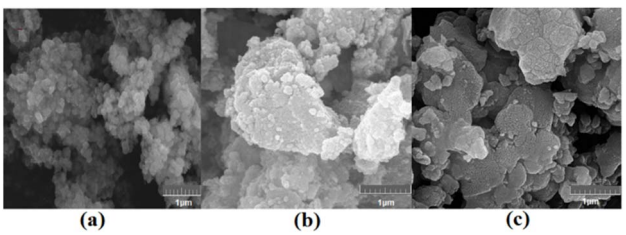

Fig. 1 SEM image of Fe_3O_4 (a), Fe_3O_4/cellulose (b), and Fe_3O_4/cellulose/Zn-MOF (c).

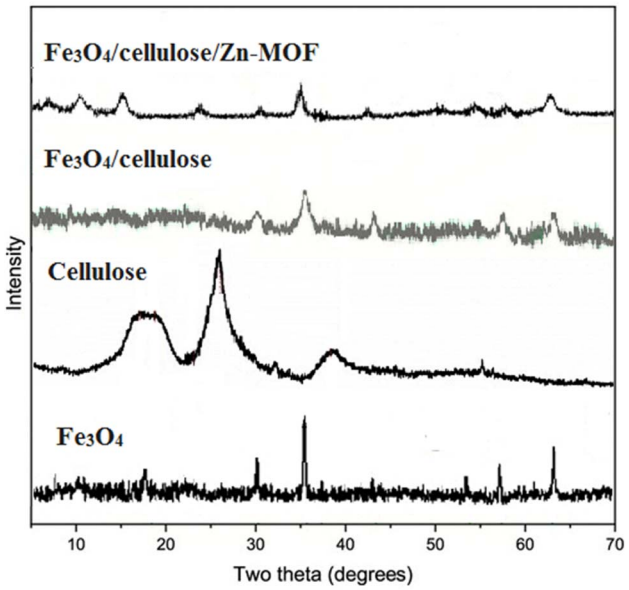

Fig. 2 XRD pattern of Fe_3O_4, cellulose, Fe_3O_4/cellulose, and Fe_3O_4/cellulose/Zn-MOF.

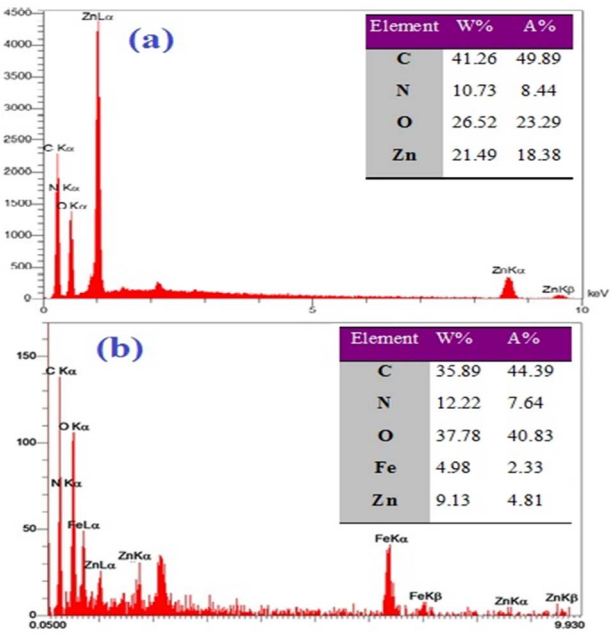

Fig. 3 EDX spectra of Zn-MOF (a) and Fe_3O_4/cellulose/Zn-MOF (b).

The FT-IR spectra for Fe_3O_4, cellulose, Fe_3O_4/cellulose,[58] and Fe_3O_4/cellulose/Zn-MOF are displayed in Fig. 5. In the Fe_3O_4 spectrum, the peaks that appeared at 568 and 3428 cm^{-1} are attributed to the Fe–O and O–H bonds, confirming the existence of hydroxyl groups on the surface of nanoparticles. A similar absorption band was also observed at 570 cm^{-1} in the Fe_3O_4/cellulose nanocomposite's FT-IR spectrum pattern. The shift observed in the Fe–O peak compared to pristine NPs indicates a strong interaction between the cellulose coating and the magnetic core. The peak around 1647 cm^{-1} can be assigned to

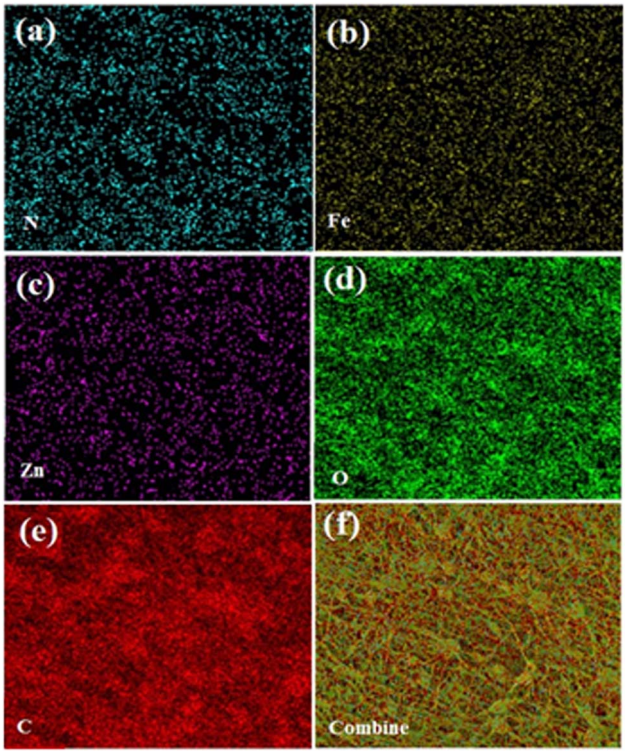

Fig. 4 EDX elemental mapping of the Fe_3O_4/cellulose/Zn-MOF.

C=N stretching vibrations. Additional absorption bands found at 2921–3430, 1436, 1378, and 1044 cm^{-1} correspond to the O–H and C–H stretching, C–H flexural/modified, and C–O flexural vibrations, respectively. In addition, the coordination peak related to the Zn–N bond can be observed in spectra at

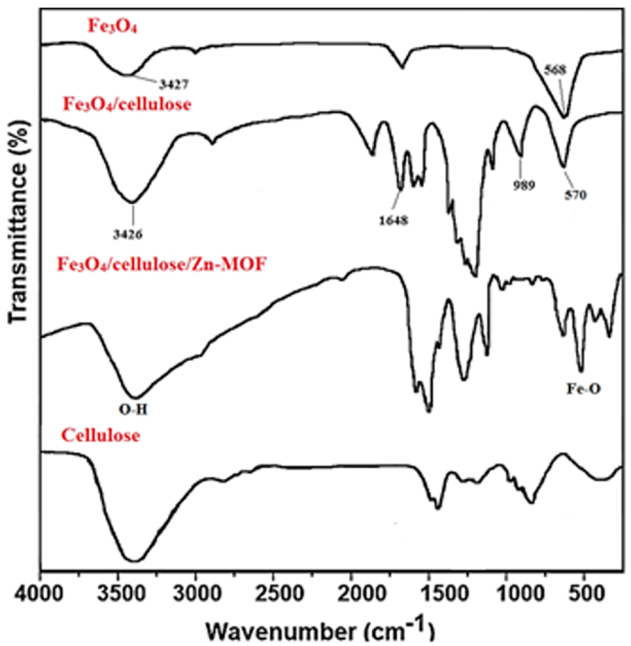

Fig. 5 FT-IR spectrum of the Fe_3O_4, cellulose, Fe_3O_4/cellulose, and Fe_3O_4/cellulose/Zn-MOF.

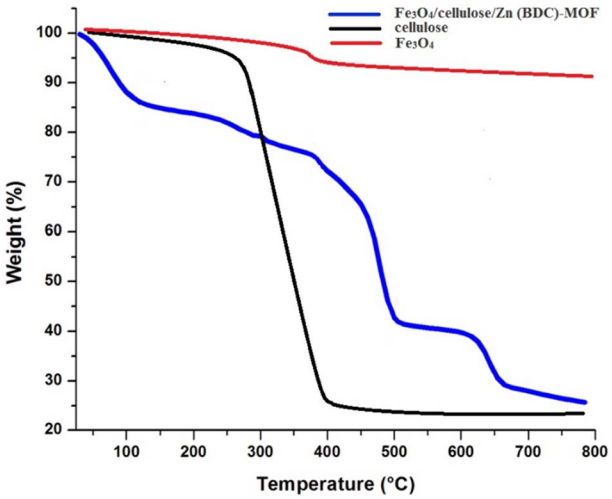

Fig. 6 TGA curve of Fe_3O_4, Fe_3O_4/cellulose and Fe_3O_4/cellulose/Zn-MOF (c).

667 cm^{-1}. In the spectral patterns shown here, the broadening of the absorption bands related to the hydroxyl group vibrations, along with their shift to lower wavelengths in the FT-IR spectrum of the synthesized nanocomposite relative to pure cellulose, can be ascribed to bond formation and interactions between the O–H groups and Fe_3O_4 NPs.

TGA was employed to measure the resistance and stability of the nanocomposites to thermal decomposition (Fig. 6). The newly synthesized Fe_3O_4/cellulose/Zn-MOF nanocomposite showed an initial weight loss near 110 °C due to the evaporated guest water molecules within the MOF pores. A progressive weight loss followed until 310 °C due to the evaporation of coordinated DMF solvent within the MOF pores. The third weight loss, between 310 °C and circa 500 °C, is due to the loss of coordination of MOF frameworks. Weight loss beyond 500 °C is indicative of the pyrolytic decomposition of the material. Overall, the thermal analysis suggests that the structural stability of Fe_3O_4/cellulose/Zn-MOF is maintained until temperatures of about 400 °C.

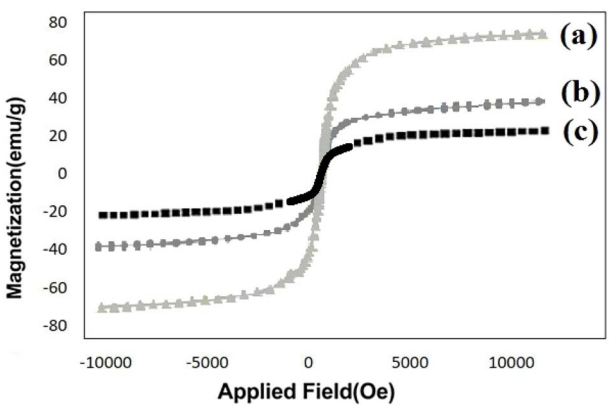

Fig. 7 VSM analysis of Fe_3O_4 (a), Fe_3O_4/cellulose (b), and Fe_3O_4/cellulose/Zn-MOF (c).

Table 1 Optimizations of the reaction conditions in the synthesis of 5-(1*H*-indol-3-yl)-7-(4-nitrophenyl)tetrazolo[1,5-*a*]pyrimidine-6-carbonitrile and 6-hydroxy-1,3-dimethyl-5-(2,4-diphenylthiazol-5-yl)-pyrimidine-2,4(1*H*,3*H*)-dione

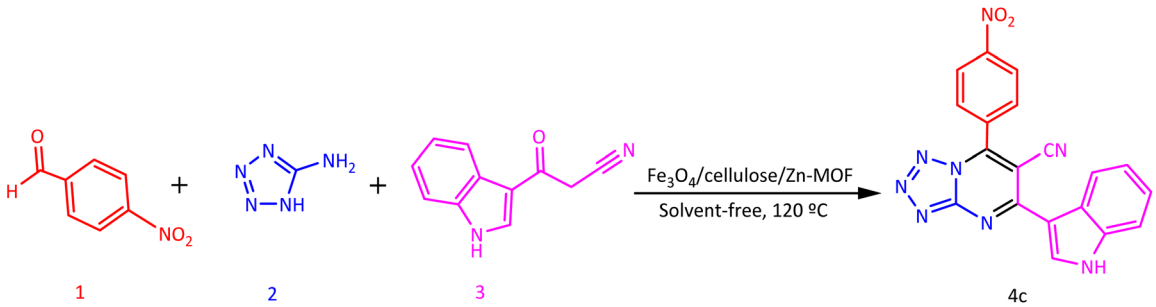

1 2 3 4c

Entry	Catalyst (g)	Solvent	Temperature (°C)	Yield[a] (%)
1	No catalyst	Solvent-free	120	No reaction
2	Fe_3O_4 (0.02)	Solvent-free	100	70
3	Fe_3O_4/cellulose (0.02)	Solvent-free	100	75
4	Zn-MOF (0.02)	Solvent-free	100	83
5	Fe_3O_4/cellulose/Zn-MOF (0.001)	Solvent-free	100	80
6	Fe_3O_4/cellulose/Zn-MOF (0.005)	Solvent-free	100	84
7	Fe_3O_4/cellulose/Zn-MOF (0.01)	Solvent-free	100	89
8	Fe_3O_4/cellulose/Zn-MOF (0.02)	Solvent-free	120	96
9	Fe_3O_4/cellulose/Zn-MOF (0.02)	Solvent-free	130	96
10	Fe_3O_4/cellulose/Zn-MOF (0.03)	Solvent-free	120	96
11	Fe_3O_4/cellulose/Zn-MOF (0.02)	Solvent-free	100	84
12	Fe_3O_4/cellulose/Zn-MOF (0.02)	Solvent-free	90	70
13	Fe_3O_4/cellulose/Zn-MOF (0.02)	Ethanol	80	61
14	Fe_3O_4/cellulose/Zn-MOF (0.02)	H_2O–EtOH (1 : 1)	80	48
15	Fe_3O_4/cellulose/Zn-MOF (0.02)	CH_3CN	80	36
16	Fe_3O_4/cellulose/Zn-MOF (0.02)	H_2O	100	Not completed

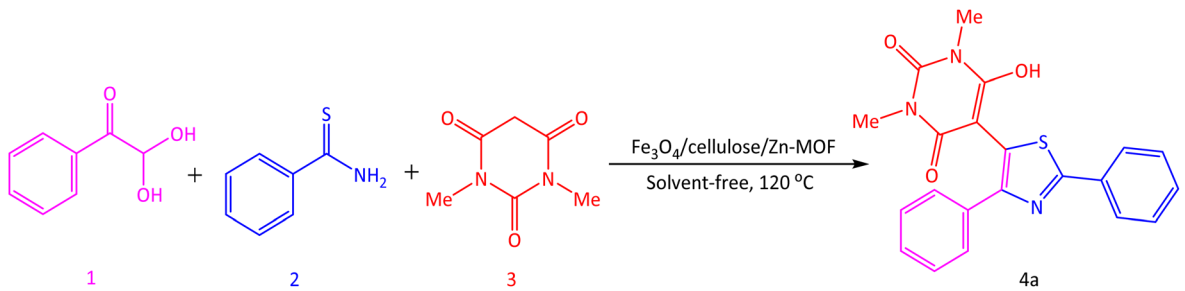

1 2 3 4a

17	No catalyst	Solvent-free	110	No reaction
18	Fe_3O_4 (0.05)	Solvent-free	100	50
19	Fe_3O_4/cellulose (0.05)	Solvent-free	100	66
20	Zn-MOF (0.05)	Solvent-free	100	73
21	Fe_3O_4/cellulose/Zn-MOF (0.001)	Solvent-free	100	80
22	Fe_3O_4/cellulose/Zn-MOF (0.005)	Solvent-free	100	84
23	Fe_3O_4/cellulose/Zn-MOF (0.008)	Solvent-free	100	89
24	Fe_3O_4/cellulose/Zn-MOF (0.05)	Solvent-free	100	92
25	Fe_3O_4/cellulose/Zn-MOF (0.05)	Solvent-free	120	95
26	Fe_3O_4/cellulose/Zn-MOF (0.05)	Solvent-free	130	95
27	Fe_3O_4/cellulose/Zn-MOF (0.08)	Solvent-free	120	96
28	Fe_3O_4/cellulose/Zn-MOF (0.05)	Solvent-free	80	86
29	Fe_3O_4/cellulose/Zn-MOF (0.05)	Solvent-free	60	71
30	Fe_3O_4/cellulose/Zn-MOF (0.05)	Ethanol	80	68
31	Fe_3O_4/cellulose/Zn-MOF (0.05)	H_2O–EtOH (1 : 1)	80	55
32	Fe_3O_4/cellulose/Zn-MOF (0.05)	CH_3CN	80	74
33	Fe_3O_4/cellulose/Zn-MOF (0.05)	H_2O	100	24

[a] Isolated yields.

Table 2 Synthesis of tetrazolo[1,5-*a*]pyrimidine-6-carbonitrile and diphenyl-1,3-thiazole derivatives using Fe_3O_4/cellulose/Zn-MOF

Entry	Product	Time (min)	Yield[a] (%)	M.P. (°C)	M.P. (°C)
1	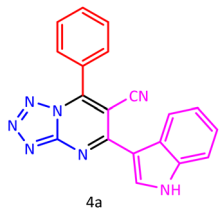 4a	20	98	249–253	250–252 (ref. 59)
2	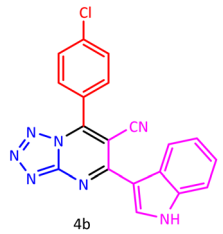 4b	16	98	275–277	276–278 (ref. 60)
3	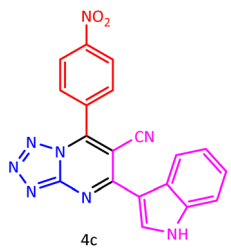 4c	15	96	287–289	286–288 (ref. 60)
4	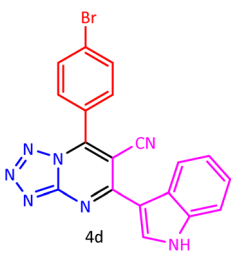 4d	16	97	280–282	279–281 (ref. 60)
5	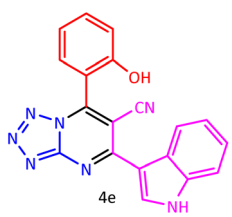 4e	20	93	271–273	271–273 (ref. 60)
6	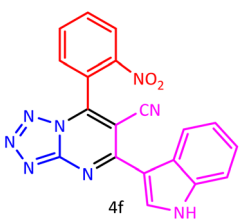 4f	18	96	290–292	291–293 (ref. 60)
7	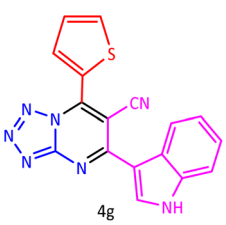 4g	20	90	268–270	266–268 (ref. 60)

Table 2 (*Contd.*)

Entry	Product	Time (min)	Yield[a] (%)	M.P. (°C)	M.P. (°C)·
8	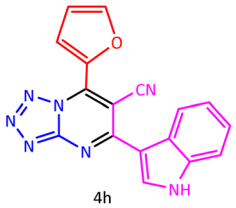 4h	20	91	265–267	269–271 (ref. 60)
9	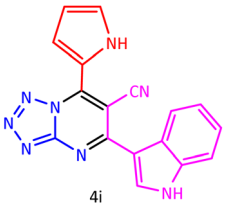 4i	20	92	257–259	258–261 (ref. 60)
10	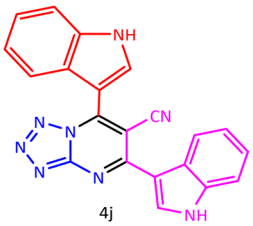 4j	20	90	297–299	296–298 (ref. 60)
11	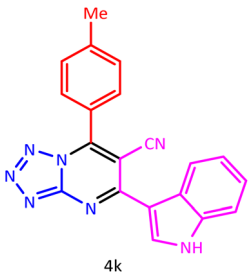 4k	17	97	289–291	289–291 (ref. 59)
12	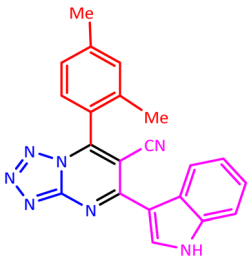 4l	16	98	276–278	276–278 (ref. 59)
13	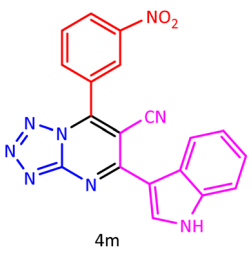 4m	18	97	283–285[b]	—

Table 2 (*Contd.*)

Entry	Product	Time (min)	Yield[a] (%)	M.P. (°C)	M.P. (°C)·
14	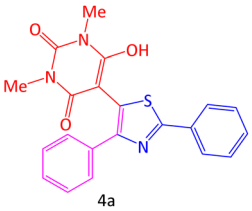 4a	30	95	265–267	265–267 (ref. 61)
15	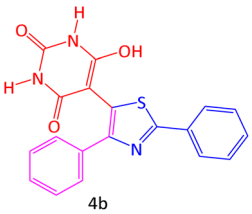 4b	35	94	326–328	325–327 ref(. 61)
16	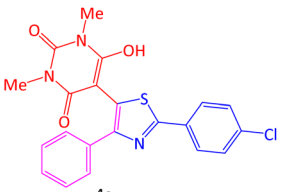 4c	40	93	260–262	260–262 (ref. 61)
17	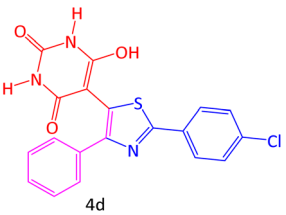 4d	45	95	329–331	328–330 (ref. 61)
18	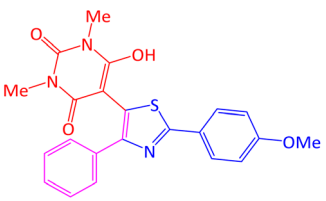 4e	40	94	260–261	259–261(ref. 61)
19	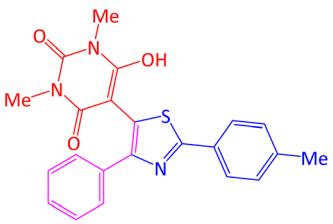 4f	48	93	269–271	270–272 (ref. 61)
20	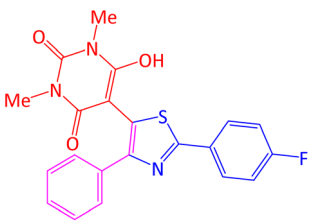 4g	35	90	247–249	247–249 (ref. 61)

Table 2 (*Contd.*)

Entry	Product	Time (min)	Yield[a] (%)	M.P. (°C)	M.P. (°C)
21	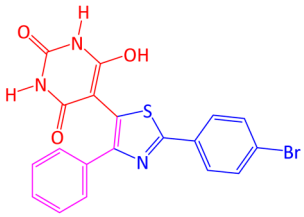 4h	40	94	311–313[b]	—
22	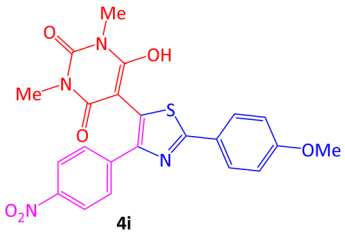 **4i**	60	96	308–310	309–311 (ref. 61)
23	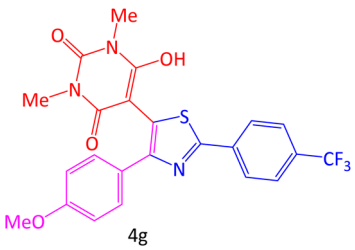 4g	30	98	240–242	240–243 (ref. 61)
24	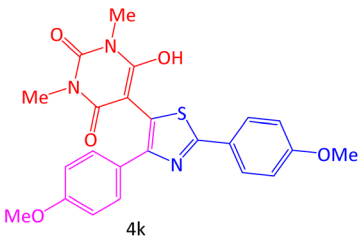 4k	30	89	257–259	256–258 (ref. 61)
25	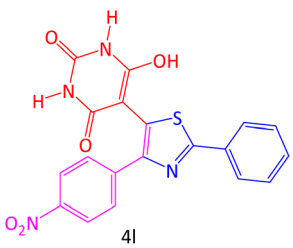 4l	30	88	301–303	300–302 (ref. 61)

[a] Isolated yields. [b] Novel compounds.

A vibrating-sample magnetometer (VSM) was used to study the magnetic properties of the materials. Fig. 7a–c gives the magnetization curves for Fe_3O_4, Fe_3O_4/cellulose, and Fe_3O_4/cellulose/Zn-MOF with saturation magnetization (M_s) values of 69.0, 38.0, and 21.0 emu g^{-1}, respectively. These curves reveal the existence of a magnetic hysteresis loop. Despite a lower M_s value in comparison with as-synthesized Fe_3O_4 and Fe_3O_4/cellulose, Fe_3O_4/cellulose/Zn-MOF still possesses a considerably high level of magnetization. Moreover, its magnetic separability was assessed by placing a magnet adjacent to a glass vial containing the sample.

Catalytic activity

Once successfully characterized, the synthesized sample's catalytic activity was evaluated by synthesizing two distinct classes of N-containing heterocycles: diphenyl-1,3-thiazoles and

tetrazolo[1,5-*a*]pyrimidine-6-carbonitriles. Two representative reactions were chosen for the optimization of the synthesis of 6-hydroxy-1,3-dimethyl-5-(2,4-diphenylthiazol-5-yl)pyrimidine-2,4(1*H*,3*H*)-dione and 5-(1*H*-indol-3-yl)-7-(4-nitrophenyl)tetrazolo[1,5-*a*]pyrimidine-6-carbonitrile. Various parameters were examined, including the catalyst type and loading, reaction temperature, and solvent absence or presence (Table 1). Initial examination of reactions performed at room temperature in the presence of different solvents did not yield satisfactory results, with significant amounts of starting materials and intermediates visible on TLC plates. A gradual increase in the reaction temperature to 120 °C under solvent-free conditions led to the highest product yield and minimized reaction times. Further, the catalyst screening for the representative reaction demonstrated that although metal NPs and acidic catalysts substantially enhanced yields, they required longer reaction times. According to Table 1, Fe_3O_4/cellulose/Zn-MOF proved to be the most efficient catalyst. As shown, optimum amounts of this nanocomposite (0.02 and 0.05 g) enabled the formation of **4c** and **4a** within 15 and 30 min, respectively (entries 8 and 24). Moreover, both catalyst-free reactions failed to proceed beyond trace levels.

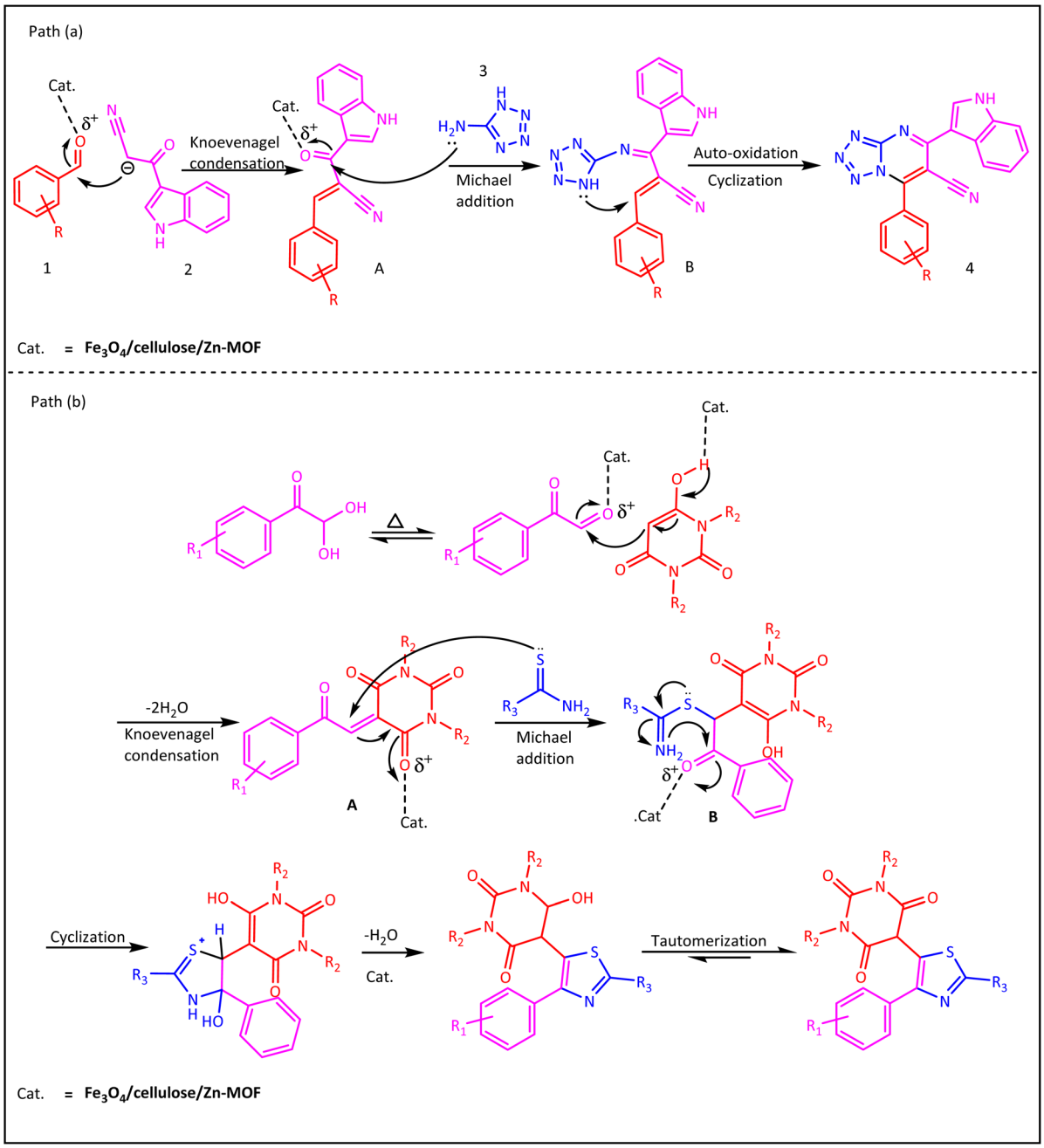

Scheme 2 The proposed mechanism for the synthesis tetrazolo[1,5-*a*]pyrimidine-6-carbonitrile and diphenyl-1,3-thiazole derivatives using in the presence of Fe_3O_4/cellulose/Zn-MOF.

To further validate the generality of the proposed method, multiple aromatic aldehydes along with various barbituric acid derivatives and/or aryl glyoxals, aryl thioamides, and *N*,*N*′-dimethylbarbituric acid were employed under optimal conditions for synthesizing their corresponding diphenyl-1,3-thiazole and tetrazolo[1,5-*a*]pyrimidine-6-carbonitrile derivatives (Table 2). As shown, the proposed method afforded all the requested products in excellent yields within short reaction times (Table 2). This process enabled the synthesis of 13 derivatives from the first MCR series and 12 from the second, including two novel compounds.

Scheme 2 presents a suggested reaction mechanism catalyzed by Fe_3O_4/cellulose/Zn-MOF. The aldehyde is activated by the Zn^{2+} ion, which serves as a Lewis acid site. Uncoordinated imidazole adsorbed in Zn-MOF serves as a base to promote the deprotonation of the methylene for the production of a carbanion. Path (a) corresponds to tetrazolo[1,5-*a*]pyrimidine-6-carbonitrile synthesis. Initially, intermediate **A** is formed by a reaction between activated carbonyl **1** and 3-cyanoacetyl indole **2**. This is followed by its reaction with 1*H*-tetrazol-5-amine **3** through Michael addition to generate the intermediate **B**, which then cyclizes intramolecularly to form a new C–N bond. Auto-oxidation furnishes the product **4**.[59,60] Path (b) presents the mechanism of the synthesis of diphenyl-1,3-thiazole derivatives. The mechanism involves a series of steps: Knoevenagel condensation, Michael addition, and intramolecular cyclization. First, the intermediate **A** was formed *via* a Knoevenagel condensation reaction between barbituric acid and aryl glyoxal. Afterward, the intermediate **B** was formed by adding thioamide to the intermediate **A** *via* 1,4-Michael addition. Finally, the final trisubstituted thiazole product was provided *via* the intermediate **B**'s intramolecular cyclization and loss of a water molecule. The reaction is facilitated by the nanocomposite catalyst with both acidic and basic surface sites by promoting acidic proton abstraction and carbonyl group activation for the nucleophilic attack. Overall, these mechanisms align well with previous studies.[61,62]

As evidenced in Table 3, the juxtaposition of our results with those reported for other catalytic systems reveals the clear advantages of the Fe_3O_4/cellulose/Zn-MOF nanocomposite. This method overcomes the persistent disadvantages of previously described procedures, such as diminished yields, cumbersome catalyst synthesis, elevated catalyst loading, and extended reaction times.

A catalyst must be efficient and cost-effective to be transitioned from laboratory scale to industrial-scale application. Owing to its considerable reusability, Fe_3O_4/cellulose/Zn-MOF could effectively participate in over 5 consecutive reaction cycles (Table 4). After each cycle, it was magnetically recovered from the reaction mixture, eluted with warm ethanol, dried, and reused for the next cycle. Remarkably, the catalyst retained its structural integrity even after multiple cycles of recovery. Over

Table 4 Reusability of Fe_3O_4/cellulose/Zn-MOF

Entry	Cycle	Yield[a,c] (%)	Yield[b,c] (%)
1	Fresh	96	95
2	1st recycle	95	94
3	2nd recycle	95	93
4	3rd recycle	94	92
5	4th recycle	93	91
6	5th recycle	91	90

[a] Reaction conditions: 4-nitrobenzaldehyde (1 mmol), 1*H*-tetrazole-5-amine (1 mmol), and 3-cyanoacetyl indole (1 mmol), Fe_3O_4/cellulose/Zn-MOF (0.02 g), solvent-free, 120 °C, 15 min. [b] Reaction conditions: phenylglyoxal monohydrate (1 mmol), 1,3-dimethylbarbituric acid (1 mmol), and thiobenzamide (1 mmol), Fe_3O_4/cellulose/Zn-MOF (0.05 g), solvent-free, 120 °C, 30 min. [c] Isolated yield.

Table 3 Comparison between reported synthetic methods and the present method for the selected compounds

Product	Catalyst [ref.]	Reaction conditions	Time (min)/yield[a] (%)
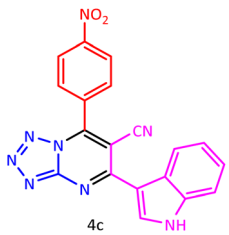 4c	UiO-66-NH_2 MOF[59]	Solvent-free/100 °C	25 min/94
	Et_3N[60]	DMF/reflux	10 h/71
	Fe_3O_4/cellulose/Zn-MOF[This work]	Solvent-free/120 °C	15 min/96
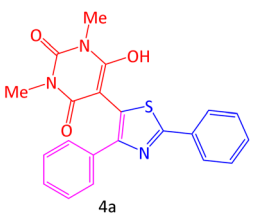 4a	HCl[61]	rt, stirring	8 h/82
	$FeCl_3 \cdot 6H_2O$[62]	DMF/60 °C	6 h/80
	Fe_3O_4/cellulose/Zn-MOF[This work]	Solvent-free/120 °C	30 min/95

[a] Isolated yield.

five runs, the reaction time and yields did not significantly change in each run.

Conclusions

According to structural studies and characterization results obtained by SEM, XRD, EDX mapping, VSM, TGA, and FT-IR, Fe_3O_4/cellulose/Zn-MOF, a magnetic nanocomposite, was successfully synthesized. This cost-effective and efficient catalyst was subsequently used at 120 °C under solvent-free conditions for synthesizing diphenyl-1,3-thiazole and tetrazolo[1,5-*a*] pyrimidine-6-carbonitrile derivatives. The synthesized nanocatalyst exhibited superior catalytic performance over previous methods, as evidenced by high product yields, short reaction times, and facile purification and isolation of the final product. It can be magnetically recovered and reused for up to five cycles with minimal loss of catalytic activity, thereby underscoring its potential for efficient, sustainable, and cost-effective heterocyclic compound synthesis.

Conflicts of interest

There are no conflicts to declare.

Data availability

The data supporting this article have been included as part of the supplementary information (SI). Supplementary information is available. See DOI: https://doi.org/10.1039/d5ra07068f.

Acknowledgements

We are thankful to the Research Council of the University of Guilan for its assistance in conducting this research.

References

1 A. Khojastehnezhad, H. Gamraoui, M. Jafari, Z. Peng, F. Moeinpour and M. Siaj, *ACS Appl. Nano Mater.*, 2023, **6**, 17706.
2 A. Khojastehnezhad, M. Rajabzadeh, M. Jafari, F. Moeinpour, R. Khalifeh, J. Huot, D. Ma and M. Siaj, *Microporous Mesoporous Mater.*, 2023, **360**, 112729.
3 F. Taghavi, A. Khojastehnezhad, R. Khalifeh, M. Rajabzadeh, F. Rezaei, K. Abnous and S. M. Taghdis, *New J. Chem.*, 2021, **45**, 15405.
4 A. M. El-Toni, M. A. Habila, J. P. Labis, Z. A. ALOthman, M. Alhoshan, A. A. Elzatahryf and F. Zhangg, *Nanoscale*, 2016, **8**, 2510.
5 S. Vaidya, K. V. Ramanujachary, S. E. Lofland and A. K. Ganguli, *Cryst. Growth Des.*, 2009, **9**, 1666.
6 S. Singh, V. Kaur and N. Kumar, *Metal Semiconductor Core-Shell Nanostructures for Energy and Environmental Applications*, 2017, vol. 35.
7 R. Singh and R. Bhateria, *Environ. Geochem. Health*, 2021, **43**, 2459.
8 S. Kargar, D. Elhamifar and A. Zarnegaryan, *J. Phys. Chem. Solids*, 2020, **146**, 109601.
9 J. Rahimi and A. Maleki, *Mater. Today Chem.*, 2020, **18**, 100362.
10 K. Karami, M. Ghasemi and N. H. Naeini, *Catal. Commun.*, 2013, **38**, 10.
11 A. Maleki, M. Niksefat, J. Rahimi and R. Taheri-Ledari, *Mater. Today Chem.*, 2019, **13**, 110.
12 A. F. Hassan and H. Elhadidy, *J. Phys. Chem. Solids*, 2019, **129**, 180.
13 S. Sajjadi, A. Khataee, R. D. C. Soltani and A. Hasanzadeh, *J. Phys. Chem. Solids*, 2019, **127**, 140.
14 *Organic–Inorganic Hybrid Nanomaterials*, ed. S. Kalia and Y. Haldorai, Springer, 2015.
15 C. Sanchez, B. Julián, P. Belleville and M. Popall, *J. Mater. Chem.*, 2005, **15**, 3559.
16 A. Kaushik, R. Kumar, S. K. Arya, M. Nair, B. D. Malhotra and Sh. Bhansali, *Chem. Rev.*, 2015, **115**, 4571.
17 L. Han, H. J. Choi, S. J. Choi, B. Liu and D. W. Park, *Green Chem.*, 2011, **13**, 1023.
18 K. Chen, W. Fan, C. Huang and X. Qiu, *J. Phys. Chem. Solids*, 2017, **110**, 9.
19 M. Zhang, Y. H. Liu, Z. R. Shang, H. C. Hu and Z. H. Zhang, *Catal. Commun.*, 2017, **88**, 39.
20 M. A. Nasseri and M. Sadeghzadeh, *Res. J. Sci.*, 2013, **125**, 537.
21 G. Gao, J. Q. Di, H. Y. Zhang, L. P. Mo and Z. H. Zhang, *J. Catal.*, 2020, **387**, 39.
22 M. N. Chen, L. P. Mo, Z. S. Cui and Z. H. Zhang, *Curr. Opin. Green Sustainable Chem.*, 2019, **15**, 27.
23 R. Gupta, M. Yadav, R. Gaur, G. Arora and R. K. Sharma, *Green Chem.*, 2017, **19**, 3801.
24 M. Gholinejad, J. Ahmadi, C. Nájera, M. Seyedhamzeh, F. Zareh and M. Kompany-Zareh, *ChemCatChem*, 2017, **9**, 1442.
25 Y. H. Liu, J. Deng, J. W. Gao and Z. H. Zhang, *Adv. Synth. Catal.*, 2012, **354**, 441.
26 M. A. Ashraf, Z. Liu, W. X. Peng and C. Gao, *Catal. Lett.*, 2020, **150**, 683.
27 D. Lisjak and A. Mertelj, *Prog. Mater. Sci.*, 2018, **95**, 286.
28 Q. Zhang, Y. H. Gao, S. L. Qin and H. X. Wei, *Catalysts*, 2017, **7**, 351.
29 R. N. Baig and R. S. Varma, *J. Chem. Soc. D*, 2013, **49**, 752.
30 S. Li, L. Zhang, L. Zhang, Y. Guo, X. Chen, R. Holze and T. Tang, *New J. Chem.*, 2021, **45**, 16011.
31 S. A. wasthi, *Mater. Today Chem.*, 2024, **35**, 101877.
32 S. A. wasthi, J. K. Gaur and M. S. Bobji, *J. Alloys Compd.*, 2020, **848**, 156259.
33 N. Amiralian, M. Mustapic, M. S. A. Hossain, C. Wang, M. Konarova, J. Tang, J. Na, A. Khan and A. Rowan, *J. Hazard. Mater.*, 2020, **394**, 122571.
34 B. Bonnemain, *J. Drug Targeting*, 1998, **6**, 167.
35 O. S. Nielsen, M. Horsman and J. Overgaard, *Eur. J. Cancer*, 2001, **37**, 1587.
36 T. A. P. Rocha-Santos, *Trends Anal. Chem.*, 2014, **62**, 28.
37 M. Mahmoudi, V. Serpooshan and S. Laurent, *Nanoscale*, 2011, **3**, 3007.

38 A. K. Gupta and M. Gupta, *Biomaterials*, 2005, **26**, 3995.
39 P. J. J. Alvarez, C. K. Chan, M. Elimelech, N. J. Halas and D. Villagrán, *Nat. Nanotechnol.*, 2018, **13**, 634.
40 S. S. Jaffar, S. Saallah, M. Misson, S. Siddiquee, J. Roslan, S. Saalah and W. Lenggoro, *Membranes*, 2022, **12**, 287.
41 L. Chen, X. Zhang, X. Cheng, Z. Xie, Q. Kuang and L. Zheng, *Nanoscale Adv.*, 2020, **2**, 2628.
42 C. P. Raptopoulou, *Materials*, 2021, **14**, 310.
43 M. S. Alhumaimess, *J. Saudi Chem. Soc.*, 2020, **24**, 461.
44 Y. S. Wei, M. Zhang, R. Zou and Q. Xu, *Chem. Rev.*, 2020, **120**, 12089.
45 A. Bavykina, N. Kolobov, I. S. Khan, J. A. Bau, A. Ramirez and J. Gascon, *Chem. Rev.*, 2020, **120**, 8468.
46 H. Konnerth, B. M. Matsagar, S. S. Chen, M. H. G. Prechtl, F. K. Shieh and K. C. W. Wu, *Coord. Chem. Rev.*, 2020, **416**, 213319.
47 S. Vásquez-Céspedes, R. C. Betori, M. A. Cismesia, J. K. Kirsch and Q. Yang, *Org. Process Res. Dev.*, 2021, **25**, 740.
48 L. M. Aguirre-Díaz, F. Gándara, M. Iglesias, N. Snejko, E. Gutiérrez-Puebla and M. Á. Monge, *J. Am. Chem. Soc.*, 2015, **137**, 6132.
49 N. Nabinia, F. Shirini, H. Tajik, M. Mashhadinezhad and M. S. N. Langarudi, *J. Iran. Chem. Soc.*, 2018, **15**, 2147.
50 M. V. Reddy, J. Oh and Y. T. Jeong, *C. R. Chim.*, 2014, **17**, 484.
51 F. Kamali and F. Shirini, *Appl. Organomet. Chem.*, 2018, **32**, 3972.
52 T. J. Zhang, Y. Zhang, Sh. Tu, Y. hang Wu, Zh. H. Zhang and F. H. Meng, *Eur. J. Med. Chem.*, 2019, **183**, 111717.
53 D. Szulczyk, A. Bielenica, A. Głogowska, E. A. Kopeć, M. Dobrowolski, P. Roszkowski, K. Stępień, A. Chrzanowska and M. Struga, *Eur. J. Med. Chem.*, 2020, **186**, 111882.
54 D. Szulczyk, M. A. Dobrowolski, P. Roszkowski, A. Bielenica, J. Stefańska, M. Koliński, S. Kmiecik, M. Jóźwiak, M. Wrzosek, W. Olejarz and M. Struga, *Eur. J. Med. Chem.*, 2018, **156**, 631.
55 A. Rajasekaran and P. P. Thampi, *Eur. J. Med. Chem.*, 2005, **40**, 1359.
56 A. Petrou, M. Fesatidou and A. Geronikaki, *Molecules*, 2021, **26**, 3166.
57 M. H. Abdollahi-basir, F. Shirini, H. Tajik and M. A. Ghasemzadeh, *J. Mol. Struct.*, 2022, **1263**, 133022.
58 Sh. Liu, L. Zhang, J. Zhou and R. Wu, *J. Phys. Chem. C*, 2008, **12**, 4538.
59 M. H. Abdollahi-basir, F. Shirini, H. Tajik and M. A. Ghasemzadeh, *Polycyclic Aromat. Compd.*, 2022, **42**, 5719.
60 M. A. A. Radwan, F. M. Alminderej and H. M. Awad, *Molecules*, 2020, **25**, 255.
61 A. Mahata, P. Bhaumick, A. K. Panday, R. Yadav, T. Parvin and L. H. Choudhury, *New J. Chem.*, 2020, **44**, 4798.
62 M. Singh, V. B. Yadav, M. Danish Ansari, M. Malviya and I. R. Siddiqui, *Mol. Diversity*, 2022, **26**, 843.